Corrosion-induced deterioration and fracture mechanisms in ultra-high-performance fiber-reinforced concretet

Construction and Building Materials 423 (2024) 135886

Contents lists available at ScienceDirect

Construction and Building Materials

journal homepage: www.elsevier.com/locate/conbuildmat

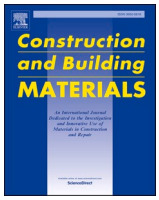

Corrosion-induced deterioration and fracture mechanisms in ultra-high-performance fiber-reinforced concretet

Zhaoping Song [a], Shaohua Li [a,*], Lulu Cheng [a], Qingliang Yu [a,b,**]

[a] School of Civil Engineering, Wuhan University, Wuhan 430072, PR China
[b] Department of the Built Environment, Eindhoven University of Technology, P.O. Box 513, Eindhoven 5600 MB, the Netherlands

ARTICLE INFO

Keywords:
Corrosion
Deterioration
Fracture mechanism
Acoustic emission (AE)
Digital image correlation (DIC)
UHPFRC

ABSTRACT

Ultra-high-performance fiber-reinforced concrete (UHPFRC) is an excellent material for harsh environments, but corrosion will change its internal microstructure and complicate the fracture evolution, bringing great difficulties in evaluating the long-term service life. Limited attention has been paid to the fracture mechanism of the UHPFRC upon corrosion. In the present study, integrating acoustic emission (AE) and digital image correlation (DIC) techniques are used to assess the micro/macrocracking characteristics of the specimens upon various corrosion degrees. Results show that the 56-day corroded UHPFRC with 2 vol% presents a remarkable decrease rate of 32%, 29% and 30% in the flexural stiffness, flexural strength and compressive strength. During the loading process, compaction of the original defects induced by fiber corrosion is concentrated in the elastic stage, the newborn cracks triggered by loading mainly occur in the strain-hardening stage, and the expansion of cracks mainly lies in the strain-softening stage. Corroded UHPFRC specimens with higher corrosion damage have a greater maximum strain value at the crack. In addition, the failure mode changes from shear crack failure to a brittle failure of tensile crack as corrosion damage increases. The macroscopic destruction of the corroded UHPFRC is a manifestation of internal microdamage evolution in fiber corrosion and matrix deterioration.

1. Introduction

Owing to its excellent durability, ultra-high performance fiber-reinforced concrete (UHPFRC) can be regarded as a sustainable building material with a wide range of applications [1–3], e.g., high-demand building, anti-explosion structures, cross-sea bridges, offshore structures, and anti-invasion structures. Steel fibers can play an effective bridging role by reducing stress concentration, limiting crack propagation in the structure and increasing energy absorption before failure [3–5]. In particular, the fracture performance in the aligned steel fiber reinforced composite is more than 80% higher than that of the random steel fiber reinforced composite [6]. However, most previous research has ignored the mechanical degradation caused by steel fiber corrosion in UHPFRC on account that fiber corrosion in UHPFRC is slow due to its very dense structure [7,8]. However, serving in marine environments, steel fiber corrosion in UHPFRC is inevitable due to iron nature being susceptible to erosion by physical and chemical absorption of mass erosive ions through the matrix. Consequently, the resulting expansive corrosion products can apply pressure on the surrounding concrete, causing the deterioration of the interface transition zone between fiber-matrix, inducing the matrix cracking along the direction of the steel fibers [9,10]. In turn, cracking and spalling of the concrete can further cause more severe corrosion of the steel fibers, triggering a reduction in the mechanical properties of the concrete structures.

For many UHPFRC structures in the course of serving lifetime, the assessment of fiber corrosion on mechanical properties is a crucial index required to determine whether the bearing capacity is guaranteed or not. Limited studies have been carried out on the damage evolution mechanisms in corroded UHPFRC. Some parameters only have been proven to affect the mechanical performance caused by corrosion in UHPFRC, including steel fiber dosages [11], accelerating time [12], immersion time [13,14] and concrete strength [15]. Yoo [14,16] adopted pre-corroded steel fiber in UHPC to investigate the mechanical properties, where the corroded steel fibers were poured into the UHPC lacking practical significance or the specimen was soaked for a long period without slight corrosion deterioration. Pyo et al. [17] evaluated the flexural behavior of steel fiber corrosion on UHPC with different thicknesses under NaCl solution up to one year. They found that fiber

* Corresponding author.
** Corresponding author at: School of Civil Engineering, Wuhan University, Wuhan 430072, PR China.
E-mail addresses: shaohuali@whu.edu.cn (S. Li), q.yu@bwk.tue.nl (Q. Yu).

https://doi.org/10.1016/j.conbuildmat.2024.135886
Received 6 January 2024; Received in revised form 5 March 2024; Accepted 17 March 2024
Available online 22 March 2024

near the concrete surface preferentially suffers from corrosion, and the deterioration of mechanical properties will occur as fiber corrosion deepens. Shin and Yoo [18] evaluated that moderate fiber corrosion would improve the tensile behavior in UHPFRC, but the performance is degraded with the increasing corrosion degree thereafter due to the fiber rupture [18,19]. Thus, to investigate the corrosion-induced deterioration in UHPFRC, electrochemical accelerated corrosion is employed [9,20,21]. In our previous studies, applying the electrochemical corrosion method, the corrosion risk and corrosion-induced deterioration in UHPFRC were well assessed [21], as well as the fiber corrosion degradation mechanism from a microscopic to macroscopic view [9]. The fiber corrosion on the strength loss has been studied, but the fundamental relationships of the cracking evolution behavior in the corroded UHPFRC have not been well-investigated thus far, especially the transition of the fracture patterns with the increasing corrosion damage.

As commonly known, the failure process in structures is complex, resulting from the occurrence of a sequence of events contained initiation and propagation of cracks, strain and local damage of materials e.g., coarse aggregate and steel fibers [4,12,22]. A better understanding of the cracking process in concrete can be achieved by a combination of digital image correlation (DIC) [23–28] and acoustic emission (AE) technique [12,15,22,29–31]. Wang et al. [12] found that AE can effectively characterize the UHPFRC matrix cracking and the de-bonding between fibers and matrix, as well as provide strong evidence for the multi-cracking in the strain-hardening stage of UHPFRC during the damage evolution process [15,29]. Lv et al. [12] found that the crack control capacity of UHPFRC decreased rapidly due to the increase of fiber corrosion, resulting in the widening of cracks, which is demonstrated by the generated AE energy due to the relieving of local stress. At the same time, using the DIC technique, Wei et al. [23,24] realized the visualization and quantification of cracking process in UHPFRC by the development of strain field. Combining the AE and DIC techniques, one can understand the micro/macro-cracking process of UHPFRC structures during loading. Flexural performance and DIC/AE monitoring have been individually applied before, but the combination of the three techniques has not been reported involving corrosion damage, leading to a high desire to investigate the deterioration and fracture evolution monitoring in the corroded UHPFRC. Furthermore, there has been no significant investigation into the comparison of various degrees of corrosion of UHPFRC specimens using both inspection approaches of AE and DIC to characterize the fracture process simultaneously.

This work aims to shed light on the corrosion-induced deterioration and fracture mechanism of the corroded UHPFRC. To achieve this task, UHPFRC with 1 vol% and 2 vol% fibers are first subjected to different corrosion degrees by electrochemical accelerated corrosion. Then, the damaged specimens are evaluated a four-point bending test. Cohesive AE and DIC analyses are employed to reveal the micro/macro-cracking time evolution of the corroded UHPFRC. The deterioration characteristics of UHPFRC upon corrosion are investigated by the mechanical property index, events analysis of AE and crack process of DIC. In addition, three-dimensional laser scanning is used to reproduce the mesoscopic surface of the deteriorated specimen. Further, the microstructure of corroded UHPFRC is observed by scanning electron microscopy (SEM). Finally, based on the acquired thorough characterization, the change in the inside microcracking paths and macroscopic failure behavior of UHPFRC exposure to various corrosion degrees are revealed.

2. Experimental description

2.1. Materials and specimen preparation

The raw materials used in this work are PII·52.5 cement, micro-silica, limestone and quartz sand, where the quartz sand is mixed with four kinds of continuous particle sizes of 124–250 μm, 250–420 μm, 420–840 μm, and 840–2000 μm, respectively. The particle size distribution of quartz sand plays a role in the skeleton in the matrix, adjusting the proportion to obtain an optimum packing. Micro-silica fills the gaps between the cement particles and promotes hydration, making the microstructure more compact. Limestone, as a role of filler, is employed to reduce the amount of binder and prevent the segregation and water seepage of the paste. The particle size distribution of the above-mentioned materials can be obtained by the methods of sieve and laser particle size analyzer (Bettersize 2000E), detail presented in Fig. 1 (d). The chemical composition and specific surface of the used powder can be found in [21,32]. The scanning electron microscopy (SEM) images of the powders are shown in Fig. 1(a-c). Based on a packing model applying the Brouwers methods [33–35], the detailed mixture proportion of UHPFRC is presented in Table 1, where a polycarboxylate-based superplasticizer with a 30% water-reducing rate is used to acquire the desired fluidity. The straight steel fibers of 0.2 mm in diameter, 13 mm in length, elastic modulus exceeding 200 GPa and tensile strength more than 2250 MPa are utilized. The optimal contents of micro-silica and limestone powder are 5% and 20% by the weight of total powder, respectively, for the aim to achieve self-compacting property in paste and ensure the homogeneous distribution of steel fibers [32]. To investigate the effects of fiber corrosion with matrix deterioration on the cracking behavior of UHPFRC, steel fibers with two volume fractions (1 vol% and 2 vol%) are applied.

The preparation of specimens is conducted as follows: 1) All the powders and sand are mixed in Hobart mixer for at least 5 min; 2) Water containing superplasticizer is poured into the mixer by two times; 3) The steel fibers are slowly added and mixed for 5 min; 4) The well-mixed mixtures are cast into the steel molds with the size of 40 × 40 × 160 mm^3, then sealed with plastic sheets immediately and stored in curing chamber at 20 ℃ and 95% RH for 24 hours. Finally, all the specimens are demolded and put into the curing chamber again for 27 days before the accelerated corrosion test.

2.2. Accelerated corrosion test setup

In order to prepare the corroded UHPFRC specimens and accelerate the corrosion development, a constant power accelerated rustler with a constant voltage of 60 v is applied. Determining by the mass loss of the corroded specimen, the corrosion time is set for 14 days, 28 days and 56 days to achieve three kinds of corrosion degrees of Low (L), Medium (M) and High (H), respectively. Corrosion is the destructive attack of steel fiber by its reaction with the corrosive environment. The schematic diagram of accelerated corrosion is shown in Fig. 1(e), using the carbon fiber cloth as the specimen conductor. The cathodic sites and anodic sites are stainless steel and carbon fiber cloth wrapped with waterproof materials, respectively. At least three specimens are measured for each group to ensure the representativeness of the results.

2.3. Four-point flexural testing

When the targeted corrosion degrees are reached, the specimens are taken out from the electrolyte and the surface is dried to conduct the four-point flexural test at a rate of 0.1 mm/min using an MTS testing machine with a maximum load capacity of 100 kN. An appropriate loading speed is crucial to the characterizations of AE and DIC. The excessively high loading rate increases the amount of instantaneous damage and cannot capture the speckle displacement clearly. In this study, considering the storage capacity of AE and DIC, 0.1 mm/min conforms to the quasi-static loading criterion and is sufficient to cover the whole fracturing process, which takes 20–30 min. According to the ASTM C1018 Standard, the size of 40 mm×40 mm×160 mm meets the requirement of small-scale concrete prisms. The designed span length (L) is set as 120 mm and the load spacing is 40 mm, conforming to the four-point loading rule of L/3 in [4,36]. The ultimate flexural strength f and normalized deflection index δ_f can be derived as follows [4]:

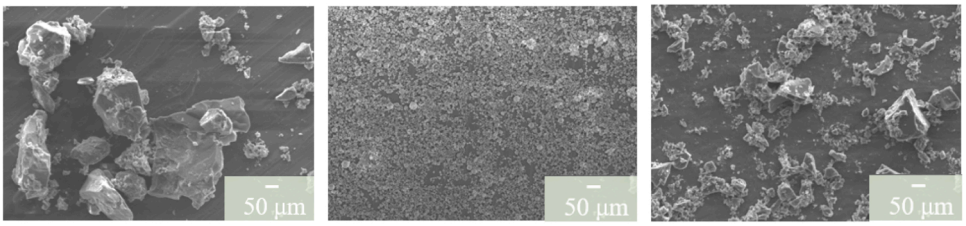

(a) PII·52.5 cement (b) Micro-silica (c) Limestone

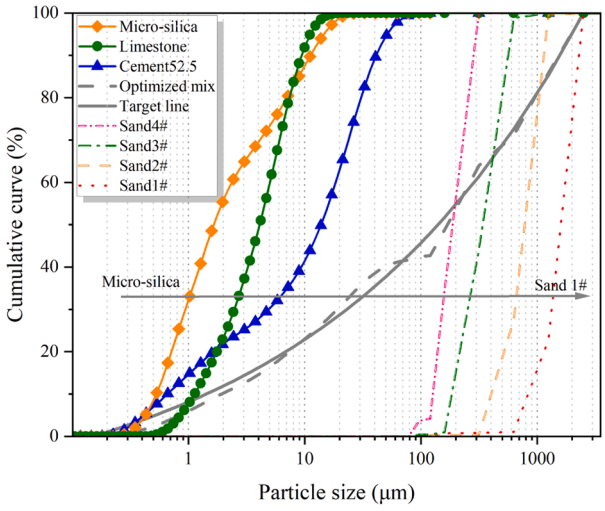

(d) Particle size distribution

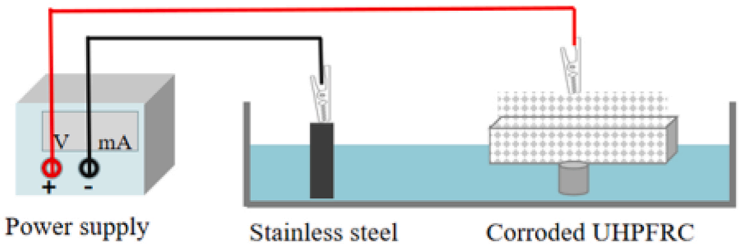

(e) Schematic diagram of accelerated corrosion in UHPFRC

Fig. 1. Illustration of the used raw materials and electrochemical methods: (a~c) SEM images of powders; (d) Particle size distribution; (e) Schematic diagram of accelerated corrosion.

Table 1
Mixture proportion of designed UHPFRC.

Quantities	cement	Micro-silica	Lime-stone powder	Super-plasticizer	Sand 1# (10–20 mesh)	Sand 2# (20–40 mesh)	Sand 3# (40–70 mesh)	Sand 4# (70–120 mesh)	Steel fibers	Water-binder ratio
Mass (kg/m^3)	712.5	47.5	190	19	483.2	338.2	132.9	253.7	1%, 2% by total volume of mixture	0.18

$$f = \frac{FL}{bd^2} \tag{1}$$

$$\delta_f = \frac{\delta}{f/f_{MOR}} \tag{2}$$

where f, f_{MOR} are the four-point flexural strength and the ultimate flexural strength (MPa), respectively; F is the imposed load (N); L, b, and d are the span length, width and height of the designed specimen (mm), respectively; δ_f is the normalized deflection index; δ is the mid-span deflection (mm).

The four-point flexural process of the specimen is divided into three stages, named Stage I/II/III, with the concrete cracking point, peak loading point and unloading point (30% of the peak load) as the boundaries. The fractured specimens are applied to conduct the compressive strength test.

2.4. AE and DIC measurements

As shown in Fig. 2, AE technology can release strain energy in the form of elastic waves, which can be applied to monitor and evaluate the damage of internal cracking, fiber rupture and the inter-facial de-

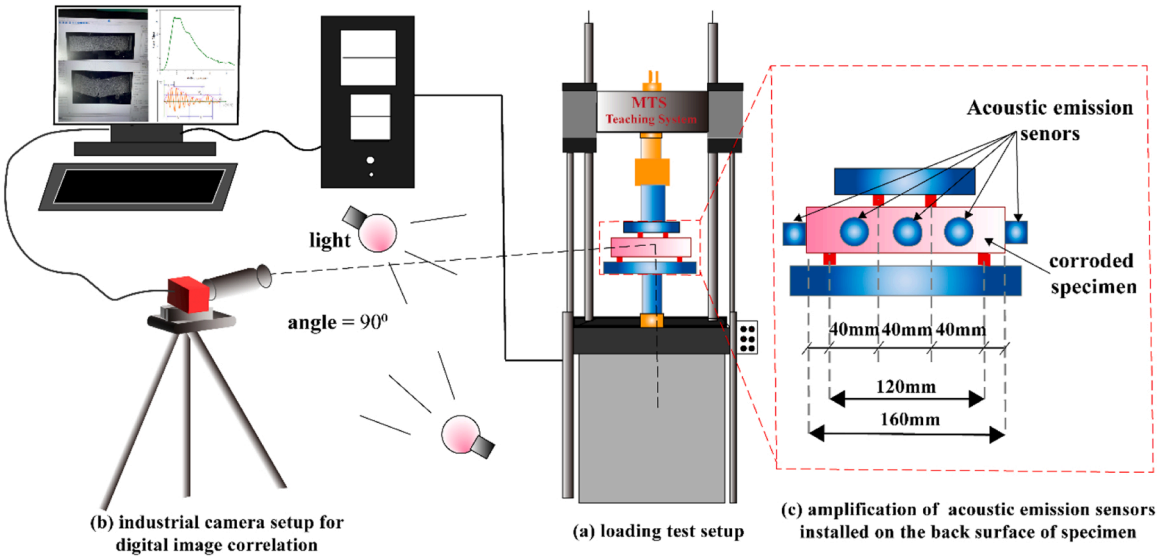

Fig. 2. Schematic illustration of a combination of digital image correlation and acoustic emission using in the corroded UHPFRC beams during four-point flexural test setup.

bonding between fiber and the surrounding concrete in real time of the corroded UHPFRC during the four-point flexural testing [12,30]. Five sensors of PCI-2 AE detection facilities with a broadband response of 40–400 kHz and a maximum sensitivity of 150 kHz, are mounted on the three-dimensional specimen surface to record the signal information produced during the loading process. In order to avoid affecting the image of cracks captured by DIC, three sensors are installed to the back sides (40 mm × 160 mm) and distributed in the center of the flexural-only and flexural-shear sections of the specimen. The distance between the three sensor centers and the near loading point is 20 mm, as shown in Fig. 2. The other two sensors are attached to the center on both sides of the specimen. A coupling agent of white petroleum jelly is employed to eliminate the air between the concrete surface and each sensor with the aim to reliably record the sound wave. All the locations contacting the senor and matrix are first polished with sandpaper, then cleaned with alcohol to prevent abnormal noise caused by friction mismatch between the senor and UHPFRC surface. Subsequently, a rubber band is used to fix the senor assembled by vacuum silicone on the specimen surface.

In AE measurement, the value of trigger threshold, frequency range and sampling rate are 35 dB, 20–200 kHz and 3 MHz, respectively. Lower signals received by the AE transducers at 30 dB is beneficial to collect the reliable low amplitude signals associated with micro-cracking in corroded UHPFRC samples. Finally, the waveform characteristic parameters of AE signal (e.g., amplitude, rising time, duration, energy count and ring count etc.) reflecting the internal damage of the corroded UHPFRC can be acquired. Energy rate of the corresponding duration can effectively discriminate the state of crack in the corroded UHPFRC during the loading process, so the energy-duration obtained by AE is analyzed. It should be noted that the energy rate value is derived from the sum of the energies of the AE events within a specified duration interval range at the corresponding stage (e.g., Stage I, II, III) of the tested specimen divided by the sum of the energies at the corresponding stage (e.g., Stage I, II, III). Further, the *RA -AF* relationship is obtained by processing the AE data, which can be used to determine the crack transition relation of the corroded UHPFRC in this work. *RA* and average frequency (*AF*) are calculated as follows by applying JCMS-III B5706 [4].

$$RA = \frac{RT}{A} \tag{3}$$

$$AF = \frac{RC}{D} \tag{4}$$

where *RT*, *RC*, *A* and *D* represent the rising time, ringing counts, peak amplitude and duration time, respectively.

Further, DIC technology can be used to determine the time of the initial crack, location and cracking direction of the UHPFRC with different corrosion degrees, and describe the whole cracking process of the corroded UHPFRC. DIC obtains the displacement vector of a pixel by tracking (or matching) the position of the same pixel in the two scatter images before and after the deformation of the corroded UHPFRC. The residue corresponds to the difference between the reference (first) image and the deformed image and is corrected for the measured displacement field to obtain the full field displacement of the sample surface. A correlation is calculated for each evaluation point, allowing the crack evolution to be followed in real-time. The specimen surface areas of 40×160 mm^2 are firstly painted with a white base layer and then sprayed with random black dots. The DIC system, as depicted in Fig. 2, comprises of two light sources, an industrial camera (MER-630–60U3M-L) and a computer to process the collected images by using an open-source code application. The camera can capture the displacement change at a maximum of 60 frames per second (fps) with a resolution of 3088 × 2064 pixels. Considering the limitation in the data storage capacity, in this work, a much lower frame rate of 0.5 seconds/picture with a resolution of 3088 × 1032 pixels, is applied to capture and record the mass image, which can cover the whole loading fracture process. In order to avoid the influence of the surrounding light changes, two independent and adjustable lights are fixed on both sides of the device during loading. Lastly, the deformation of the corroded UHPFRC under different load levels can be obtained by processing the collected images through MATLAB software.

2.5. Mesoscopic and microscopic testing

To evaluate the surface deterioration on the corroded UHPFRC, a three-dimensional laser scanning technology is employed. The specimen is placed on the scanning plate. Upon the laser scanner, the 3D coordinates of each point of the corroded UHPFRC specimen are first obtained, and a point cloud file is generated by the scanning system software. Then the camera's height and focal length are adjusted in real-time to get a clear and visible image, rotating 4–5 times until a complete surface image is realized. A solid model of the corroded specimen is

established using the software of GigE IP Configurator to post-process the scanned images which can obtain the real condition in the corroded UHPFRC under different corrosion degrees, as shown in Fig. 4 (a).

The single steel fiber and the cross-section of interface between steel fiber and matrix are cut from the split sample section with the aim of characterizing the micro-structure, as presented in Fig. 3. A single corroded steel fiber is removed from one corroded sample of each type of the designed UHPFRC specimen by a diamond saw. Then, the corroded steel fiber is soaked in an acidic solution with a concentration of 10% for one hour, cleaned with alcohol in the ultrasonic cleaner and dried in the oven at 50 ℃ for at least 48 h. Meanwhile, a block sample of 20 × 20 × 10 mm^3 is cut from the split specimen section, polished down to 0.2 μm with sandpapers (400, 800 and 1200 mesh) and polishing cloth (9, 3, 1 μm) to achieve a smooth surface, cleaned with alcohol by an ultrasonic cleaning instrument and dried in a vacuum oven until SEM analysis. Subsequently, the spraying coating of gold is applied to improve the quality and resolution of image. The micro-structure is observed by a TESCAN MIRA3 analyzer equipped with an accelerating voltage of 30 kV.

3. Results and analysis

3.1. Surface damage and compressive strength loss

Fig. 4 presents the results of corrosion-induced surface deterioration, weight loss and compressive strength variation of all corroded UHPFRC. It is clear that the matrix damage of UHPFRC presents an increasing trend with the increased corrosion time and fiber contents (Fig. 4(a)). Steel fibers located in the surface are preferentially corroded under the coupling effect of corrosive solution and impressed current, which is attributed to the small thickness of the covering layer. Thus, bubbles and rust appear on the concrete surface during the process of corrosion, indicating the serious occurrence of corrosion [37]. The corrosion area is expanded that causes a looser structure or even spalling of concrete cover. In the case of U2-H, the surface spalling is more obvious which results in a rough surface and the appearance of bare fine aggregates, presented in Fig. 4(a).

The weight loss of material can be used to determine the corrosion degree [38,39]. As corrosion deepens with the continuous invasion of corrosive solution, the weight loss and compressive strength decrease obviously, as observed in Fig. 4(b, c). The greater corrosion degree, the higher decline in compressive strength of the corroded UHPFRC is observed. The compressive strength of U2-H (6.1% weight loss) decreases to 86.13 MPa, showing a lower strength reduction than those of specimens of U2-M (weight loss of 3.8%) with 100.33 MPa and U2-L (weight loss of 1.9%) with 114.78 MPa. The strength reduces by 25% at U2-H and 12.6% at U2-M compared with U2-L. While the UHPFRC specimens with a weight loss of 1.6% (U1-L), 2.5% (U1-M) and 5.6% (U1-H) still have a reduction on the compressive strength to 95.15 MPa, 84.8 MPa and 73.03 MPa, showing a reduction up to 23.2% at U1-H and 10.9% at U1-M compared with U1-L. It can be concluded that the weight loss induced by the fiber itself corrosion and the local cross-section loss at the cover would result in the further degradation of mechanical properties of UHPFRC [40]. A high fiber content will accelerate the corrosion development under the same corrosion duration [9], resulting in a more obvious decline in the compressive strength of UHPFRC. Apparently, the compressive strength of U2-H still decreases by 8% than U1-H, compared with those subjected to the corrosion period of Low. It can be attributed to the connected 3D fiber network and the introduction of a larger interfacial zone [9,11], which accelerates the flow of erosive solution containing chloride ions and the communication of impressed current.

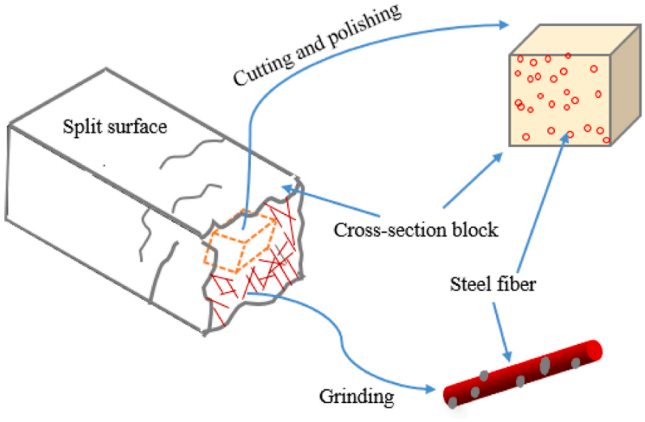

Fig. 3. Schematic illustrations for SEM imaging sampling.

3.2. Load-deflection analysis

Fig. 5 exhibits the load-deflection curves of the tested specimens with two fiber content at three corrosion degrees of Low, Medium and High up to 5 mm. The load-deflection curves of UHPFRC specimens subjected to corrosion damage are divided into three stages in sequence: Stage I (linear segment, concrete cracking acts as the terminal point), Stage II (strain-hardened segment with appearance of cracks, the stage between concrete cracking point and peak loading point), and Stage III (strain-softened segment, unloading stages).

The flexural stiffness (slope of the curve at stage I, kN/mm), toughness (the area of load-deflection curve, J), strength and defelction at point of LOP (the first cracking point, referred to the limit of proportionality, LOP) and MOR (the modulus of rupture, MOR) are also summarized in Fig. 6. At the same steel fiber content, the value of LOP and MOR on the designed UHPFRC specimen show a decreasing trend with the increasing corrosion deterioration (Fig. 6(a)). Clearly, with the increased corrosion duration from 14-day (L) to 56-day (H), the value of LOP and MOR at U1 specimens is reduced from 12.12 MPa to 8.69 MPa and 14.56 MPa to 10.47 MPa, where the decline is up to about 28%. Meanwhile, the value of LOP and MOR at U2 specimens show a reduction from 14.88 MPa to 11.65 MPa and 19.98 MPa to 14.26 MPa, respectively, with the increased corrosion degree.

As shown in Fig. 6(b), toughness of $T_{1.2}$, $T_{2.4}$ and T_5 are described as the area measured up to L/100 (1.2 mm), L/50 (2.4 mm) and L/24 (5 mm), respectively. It is clear that the toughness of $T_{2.4}$ reduces from 17.1 J to 12.4 J with the increasing corrosion degree at U2 specimen, showing a decrease up to 27.5%. At the points of $T_{1.2}$, $T_{2.4}$ and T_5, with the increasing corrosion damage from low to high, the toughness of U1 descends from 6.4 J to 4.4 J, 14 J to 8.8 J, 20.9 J to 14 J, respectively, showing a reduction rate in the range of 31.2~37.1%. The toughness of specimen at the deflection point of 1.2 mm, 2.4 mm and 5 mm present a downtrend with the growing corrosion damage, suggesting that the premature cracking of the corroded specimen due to the corrosion-induced degradation in the matrix and steel fiber. With the increase of corrosion damage, the flexural stiffness of the tested UHPFRC decreased from 18.5 kN/mm to 13.2 kN/mm (Fig. 6(b)) at 1 vol%, 20.6 kN/mm to 14.1 kN/mm at 2 vol%, getting a reduction up to 28.6% and 31.6%, respectively.

It can be attributed to that corrosion damage of steel fiber in UHPFRC has a remarkable impact on the deformation of flexural-deflection by decreasing the effective areas of steel fibers [17,41], weakening the bond-slip performance of fiber-matrix, resulting in a rapid cracking and failure. The increased corrosion damage also reduces the first cracking strength and the ultimate strength of UHPFRC, where the lowest strength is observed in the senario of corrosion degree High (Figs. 5 and 6). These results indicate that fiber corrosion has strong adverse effects on the deformability of UHPFRC at the strain-hardening stage.

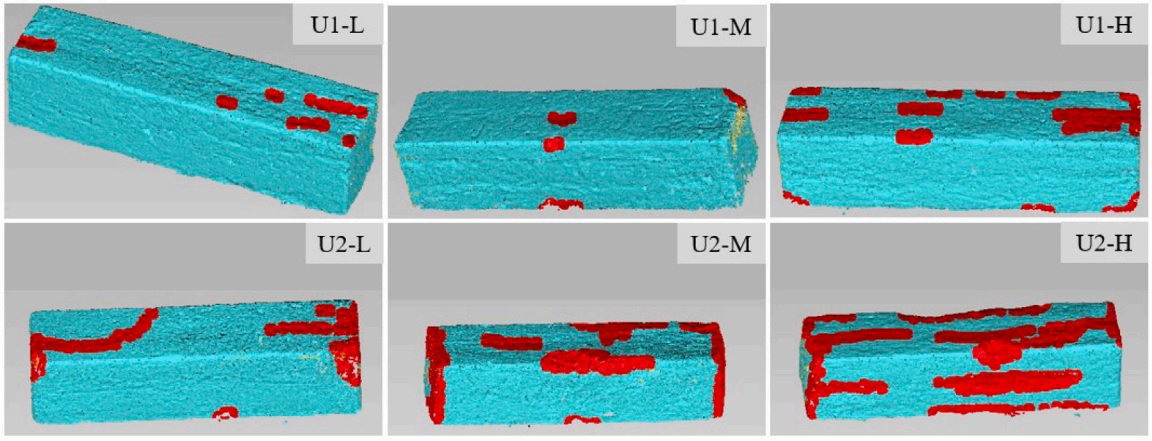

(a) 3D free scan pictures of the actual corroded specimen

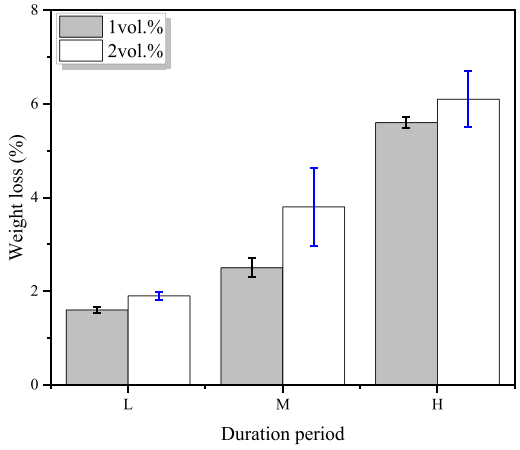

(b) The weight loss in the specimens

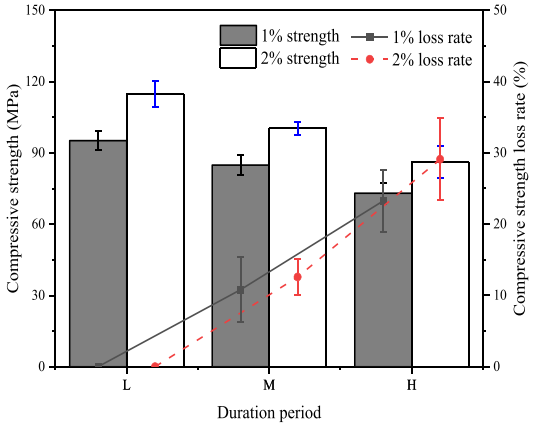

(c) The values of compressive strength and strength loss in designed specimens

Fig. 4. Implication of fiber corrosion on the matrix damage and compressive strength of the designed UHPFRC specimen.

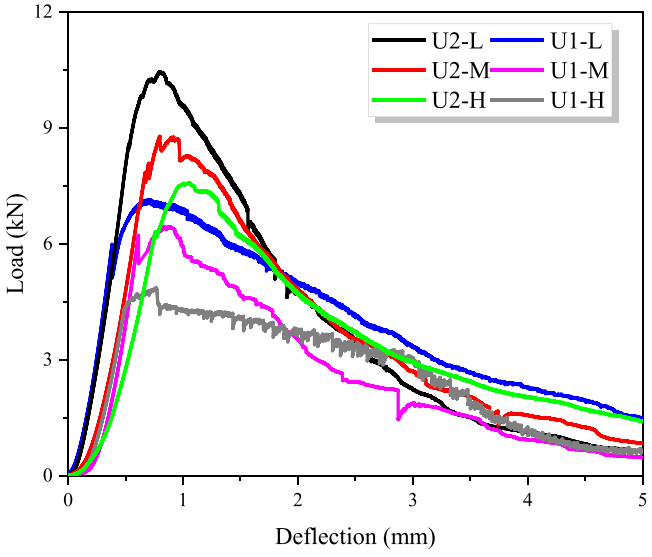

Fig. 5. Load-deflection curves of the corroded UHPFRC with two fiber content at three corrosion degree under four-point bending test.

3.3. AE characteristics

Fig. 7 illustrates the curves of ringing counts, cumulative ringing counts and load over time for the corroded UHPFRC, which can be used to assess the severity of the AE source during the deformation process. Regardless of the fiber contents, the trend of cumulative ringing counts for the three types of corroded UHPFRC are basically same to the curves of load over time, which can be divided into three stages: slow stage from the initial loading, rapid ascent stage between points of cracking and peak load, then gentle ascent at the stage of strain softening until the end of loading. The cumulative AE counts of all specimens before cracking are at a low level, which is attributed to the fact of initial compaction [42,43] and the absence of crack damage to the specimens, showing no obvious AE signals. After cracking, a large amount of AE signal originating from the degraded matrix cracking and the pull-out of steel fibers [44] or the breakage of corroded fibers, was continuously released from the concrete, leading to a sharp increase in the cumulative AE counts for all the designed specimens. Micro-cracks induced by the propagation of the macro crack contribute to the AE events at a stable status [44]. With the increased corrosion degree, in addition to the continuous fiber corrosion, the surrounding matrix inevitably would be subjected to deterioration, resulting in a smaller reduction in cumulative AE counts. When the corrosion degree is relatively low, the AE signal

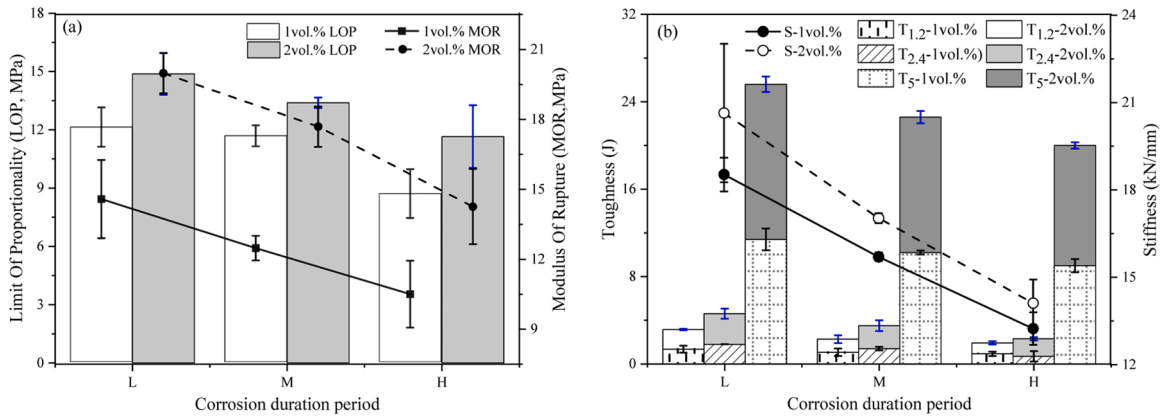

Fig. 6. Summary diagram of mechanical property index; (a) Strength values at points of LOP and MOR, (b) Flexural stiffness and flexural toughness.

mainly comes from the continuous pulling out of steel fibers. At a larger steel fiber content, the more obvious AE signal is displayed, for instance, the AE counts of U2-L are stronger than U1-L. However, when UHPFRC specimen continues to corrode and deteriorate, not only the steel fiber's stiffness decreases (Fig. 6(b)), but also the surrounding matrix starts to loosen, resulting in cracks directly go through the matrix or the deteriorated steel fiber. The more steel fiber, the more serious corrosion and deterioration of the specimen, and the AE signal is greatly reduced, for instance, that specimen of U2-H is significantly lower than U1-H, or even far lower than U2-L.

The energy-duration can be used to effectively distinguish crack modes [43,44], where nascent cracks are mainly concentrated at lower duration (e.g., 2×10^3 μs), while the propagation of existing cracks tends to develop towards longer durations (e.g., 10^4 μs) [4,43]. Based on this, the cracking behavior of corroded UHPFRC is characterized in Fig. 8. In this paper, the duration below the critical value of 10^4 μs is defined as the emergence of newborn cracks or the compacting closure of the initial micro-cracks, while the signal larger than the critical value is defined as the expansion of existing cracks. During stage I, each corroded specimen maintains a similar shorter energy-duration distribution trend. Stage I is mainly based on the initial compaction [42], where stresses are applied to some micro-cracks present in the specimen itself to close the defects. Note that the energy rate in the duration interval range of 0–500 μs at stage I shows an increasing trend with the increased corrosion deterioration. This is due to that the initial micro-defects tend to worsen with the deterioration of corrosion damage [21]. At stage II, newborn crack dominates, and with the deterioration of corrosion development, part of the acoustic energy is concentrated in the lower duration interval due to the cracks going through corroded steel fiber and penetrating the deteriorated matrix quickly. This is due to matrix deterioration caused by steel fiber corrosion, resulting in the loss of bearing capacity and the passing of the concentrated stress through the damaged matrix rapidly. When the corrosion degree reaches the medium level, the proportion of acoustic energy grouped in the duration interval above 2×10^3 μs is considered to be the highest in the phenomenon of the expansion of existing cracks. During stage III, the acoustic energy of all corroded specimens mainly shifts to a higher duration, which is dominated by the expansion of the main crack. As the steel fiber content increases, the corrosion develops even faster, causing a significant decrease in the acoustic energy. The acoustic energy of the U1-L and U2-L specimens was almost distributed in the region of $> 10^4$ μs. While the percentage of acoustic energy distributed within the duration region 10^4 μs is slightly small in the specimens of U1-M, U2-M, U1-H and U2-H, accounting for 39%, 30%, 25% and 20%, respectively. The expansion of the main crack in stages II and III is partly due to the stretching and pulling-out of the uncorroded steel fiber. These results manifest that, with the corrosion deterioration of UHPFRC, the frequency of new crack formation is higher in stage II, while the expansion acoustic energy of existing cracks is less significant. With the progress of loading, the cracks quickly move through the corroded area to the internal non-corroded fibers, increasing the acoustic energy ratio of the existing cracks. At the unloading stage III, the propagation ratio of the existing crack in the corroded specimen increases significantly, which is attributed to the weak bonding interface of the deteriorated fiber-matrix. It has been proved that the deteriorated matrix and corroded steel fibers can affect the distribution of AE energy in duration during the four-point flexural loading.

Fig. 9 depicts the RA-AF relationship. A slope line with an AF/RA ratio of 1 kHz·V/ms is taken as the limit for differentiating the type modes of shear and tensile crack according to different features [4,45–48]. The occurrence of tensile cracking accompanies by a large deal of energy released at a short time, characterized by the AE signals at a higher amplitude and ringing counts. While, the signals at a low ringing count, long rise time and duration time can be considered as shear crack [49,50]. The occurrence of fiber pull-out and sliding contributes to the AE events of shear cracking mode [51]. The proportion of shear cracks gradually decreases with the increase of corrosion deterioration (Fig. 9). While the proportion of tensile cracks increases, showing an obvious brittle failure mode due to the matrix deterioration influenced by fiber corrosion and fiber fracture. Compared to the slightly corroded specimens of U1-L and U2-L, the ratio of shear cracking on heavily corroded UHPFRC is 71.2%, 61.6%, 79.9% and 72.7% for the U1-M, U1-M, U2-H and U2-H, respectively. The steel fiber without corrosion can play a powerful bridging action, showing greater acoustic emission energy than the matrix cracking [52]. However, due to the continuous fiber corrosion, the complete steel fiber pulling out rarely occurs, and the main occurrence is the bond failure between the corroded steel fiber and the deteriorated matrix. As the steel fiber corrosion increases, and the more serious corrosion occurs in the deteriorated matrix, the greater brittle failure of tensile cracking is observed in the matrix. Corrosion damage would trigger fiber fracture and expand into the surrounding matrix, which would result in a reduction in bearing capacity and stiffness. Thus, the cracks directly pass through the matrix, generating more AE signals of tensile cracking. In addition, the shear cracking in specimens of U2 is bigger than the U1 specimen under the same corrosion damage, of which the proportion of shear crack in U2-H (72.7%) is about 18% higher than that of U1-H (61.6%). A higher steel fiber content would accelerate the corrosion development as the well connection triggers electrochemical corrosion [9,21,53]. But the large amount inside fibers still provides a strong bridging effect, where a large number of AE signals about shear crack damage occur. From the above analysis, it can be summarized that the corrosion degree of UHPFRC from slight to heavy is responsible for the transition of failure mode from shear to tensile.

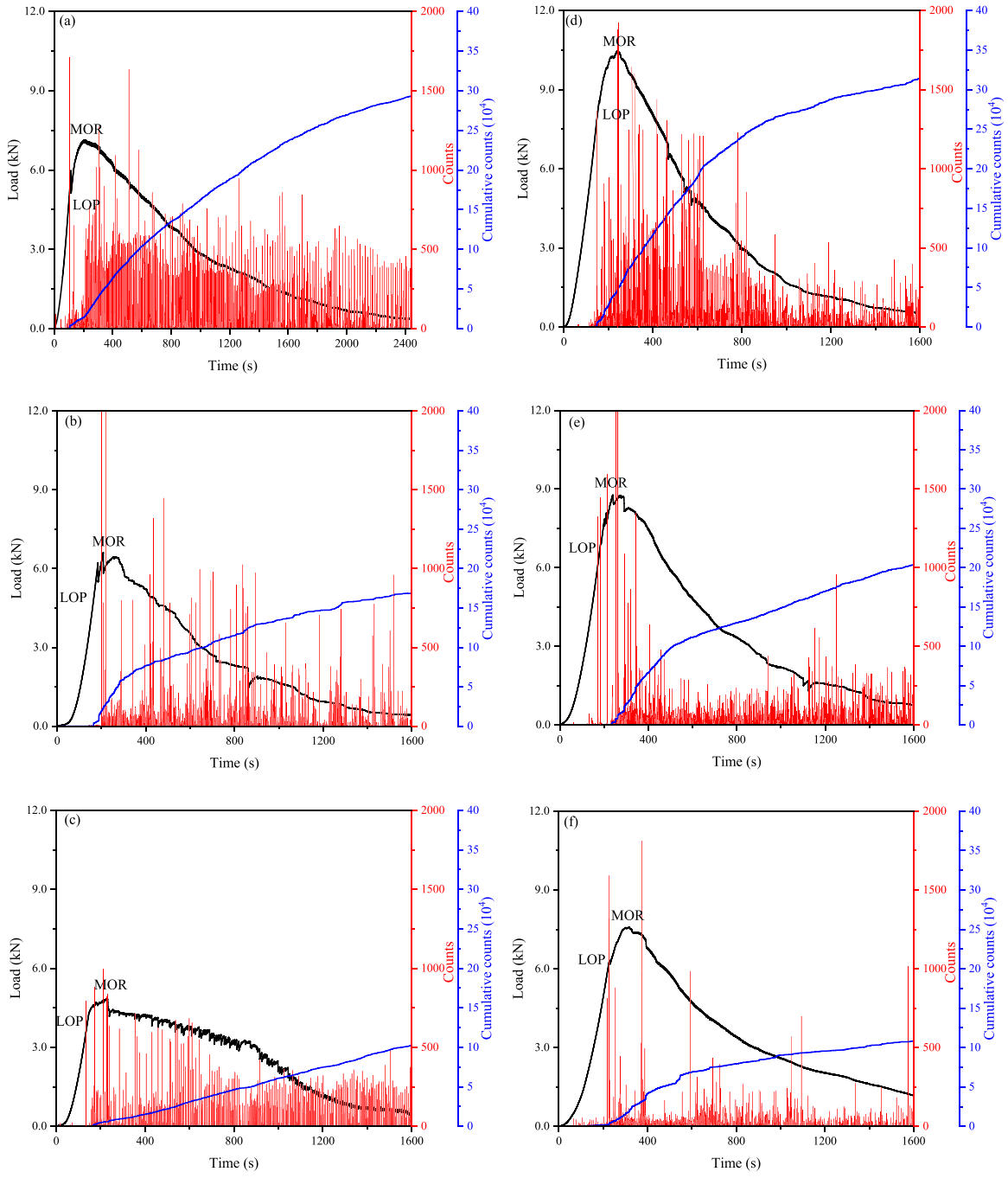

Fig. 7. Ringing counts history of corroded UHPFRC during four-point flexural deformation; (a) U1-L, (b) U1-M, (c) U1-H, (d) U2-L, (e) U2-M, (f) U2-H.

3.4. DIC analysis

To investigate the crack evolution process of the designed UHPFRC being subjected to flexural loading (Fig. 5), Fig. 10 shows the DIC observation at the interest region of P_{LOP}, P_{MOR} and 30% P_{MOR} (30% peak loading). Previous studies have reported that the strain concentration area of the concrete without corrosion will correspondingly decrease with the increase of steel fiber content, as steel fibers can effectively transfer the stress to a larger area to reduce the stress concentration [23]. Once UHPFRC is subjected to corrosion damage, the strain field will vary with the corrosion degree. Obviously, the concentration and width of strain tip of each corroded specimen change significantly with loading, showing an increasing trend, in which the strain of U2-H gradually extends upward with loading, and the strain increases from the bottom to the upper part of the specimen at the point of 30% peak load. Note that two specimens of U1-L and U2-L have reached 0.01 and 0.02 at the peak loading, whereas the main crack of U2-H show high values of 0.2. By comparing the strain fields of the desighed specimen U1-L with those of U2-L and U2-H at points of 30% P_{MOR}, it is found that the strain concentration area increases as the increase of corrosion damage [54], showing the strain values of 0.06, 0.4 and 0.8, respectively. It is concluded that the corroded UHPFRC specimens with higher corrosion damages may have bigger maximum strain value at the crack [54]. This is attributed to the loss of the ability of the corroded steel fibers to distribute the concentrated stress, and also the reduced integrity of the surrounding matrix caused by the force of corroded fiber's rust. The more fiber contents, the more serious corrosion development is, due to the easy electrochemical corrosion in the

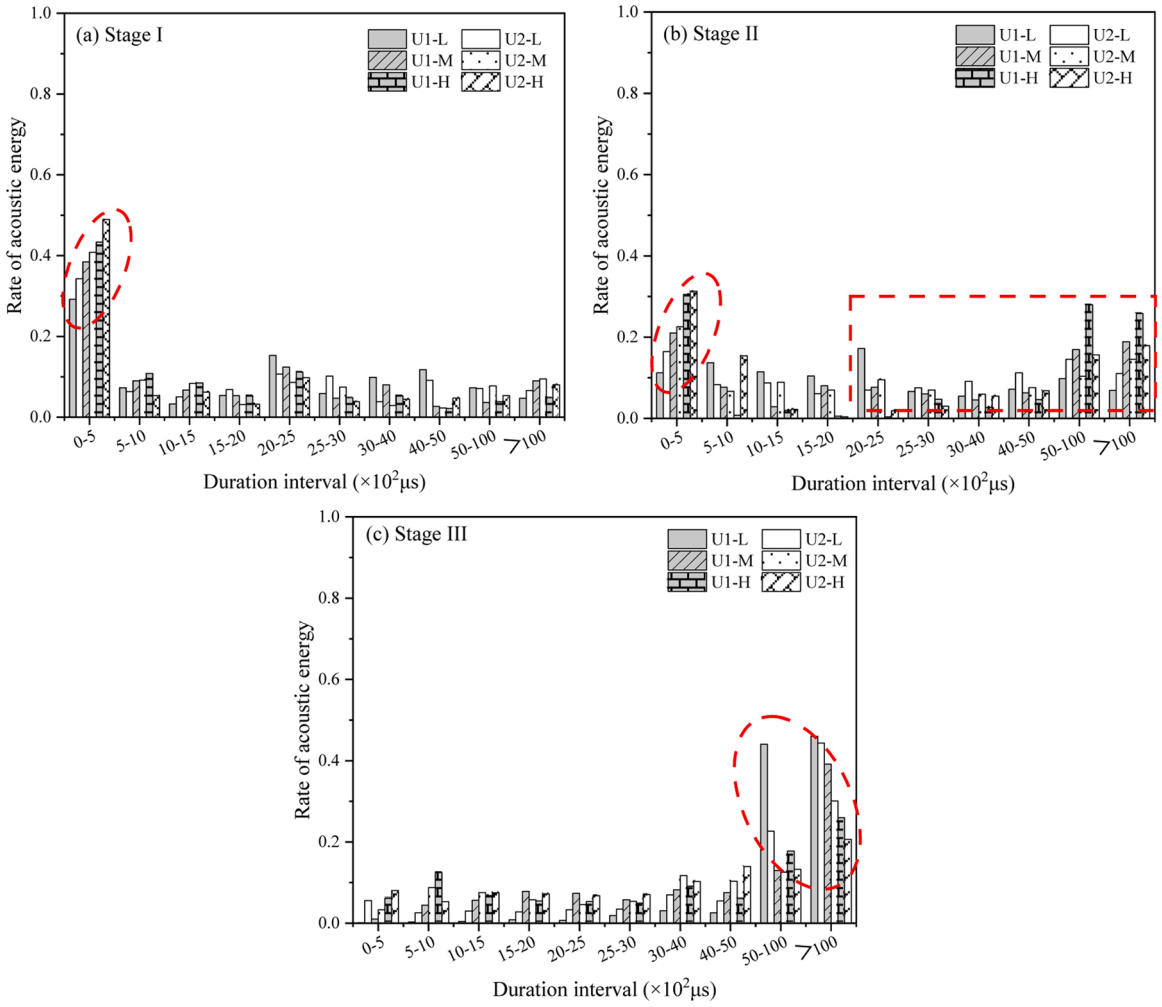

Fig. 8. Energy-duration distributions of corroded UHPFRC at different stages of I, II and III during four-point flexural deformation.

case of well connection [9,11].

3.5. Microscopic observation upon corrosion

3.5.1. Surface morphology of steel fiber

As indicated in Fig. 11 (U1-L, U1-M, U1-H, U2-L, U2-M, U2-H), the surfaces of the steel fibers show varying degrees of deterioration. At the same corrosion degree, more severe deterioration is occurred in U2 specimens. For instance, the samples of U2-L, U2-M and U2-H show a bigger deterioration than U1-L, U1-M and U1-H, respectively, due to the well connection network in specimen with the high fiber dosage that would trigger more easily electrochemical corrosion and expand the corrosion deterioration [9,21]. These microscopic images indicate that with the increased corrosion time, serious deterioration occurs on the surface of the steel fiber due to the oxidation reaction induced by erosive solution [55], forming hydrated iron oxide which is continuously adhered to the fiber surface. At lower corrosion levels (e.g., U1-L), the surface of the steel fibers is covered by the formed iron oxide and there is no significant deformation. The corrosion layer on the fiber surface of U2 specimen increases with the increased corrosion degree in accordance with U-H > U-M > U-L, causing the fiber to loosen (U2-L and U2-M) or even fracture (U2-H), leading to a significant decline in the stiffness of the fiber itself and the whole structure (Fig. 11). Therefore, the formation and development of the surface corrosion would increase the roughness of the steel fibers and expand the corrosion deterioration, and the effective volume of the steel fibers decreases due to iron oxidation.

3.5.2. Microstructure of steel fiber-matrix interface

Fig. 12 presents the microstructure of steel fiber-matrix interface. With the increased corrosion time and steel fiber contents, the deterioration of steel fiber (dissolution, splitting and fracture) and surrounding matrix (expansion of the existing cracks and new-born crack) can be clearly observed. Regardless of corrosion duration, the fiber-matrix interface of specimen with low fiber content of 1 vol% is more compact than that specimen with 2 vol%, which is attributed to the lower interface porosity in those specimen with lower fiber contents [9,21,32,56]. The more fiber contents induce more weak point for the erosive solution to invade the steel fiber [21,57], resulting in more cracks in U2 specimens than those specimens of U1 at the same corrosion degree. Also, higher fiber contents would accelerate the electrochemical corrosion which in turn expand the original weak interface [21], causing the greater deterioration in surrounding matrix with increased crack width. More increased cracks are clearly shown in U2-M and U2-H compared with those specimens of U1-M and U1-H. Corrosion would trigger the decrease of Fe/O atomic ratio [9], which is associated directly with the invasion of O_2, resulting in that elastic modulus and nano-hardness of fiber and matrix decrease with the increase of fiber contents and corrosion degree. Deterioration would be more serious with the increased corrosion time [12], the deterioration of the fiber-matrix interface follows the corrosion degree order High > Medium > Low in this work. The specimen of U2-H is the most seriously damaged, and a large number of microcracks is observed. Some cracks would directly travel through the corroded fiber due to that corrosion would destroy the integrity and stiffness of fiber itself. These

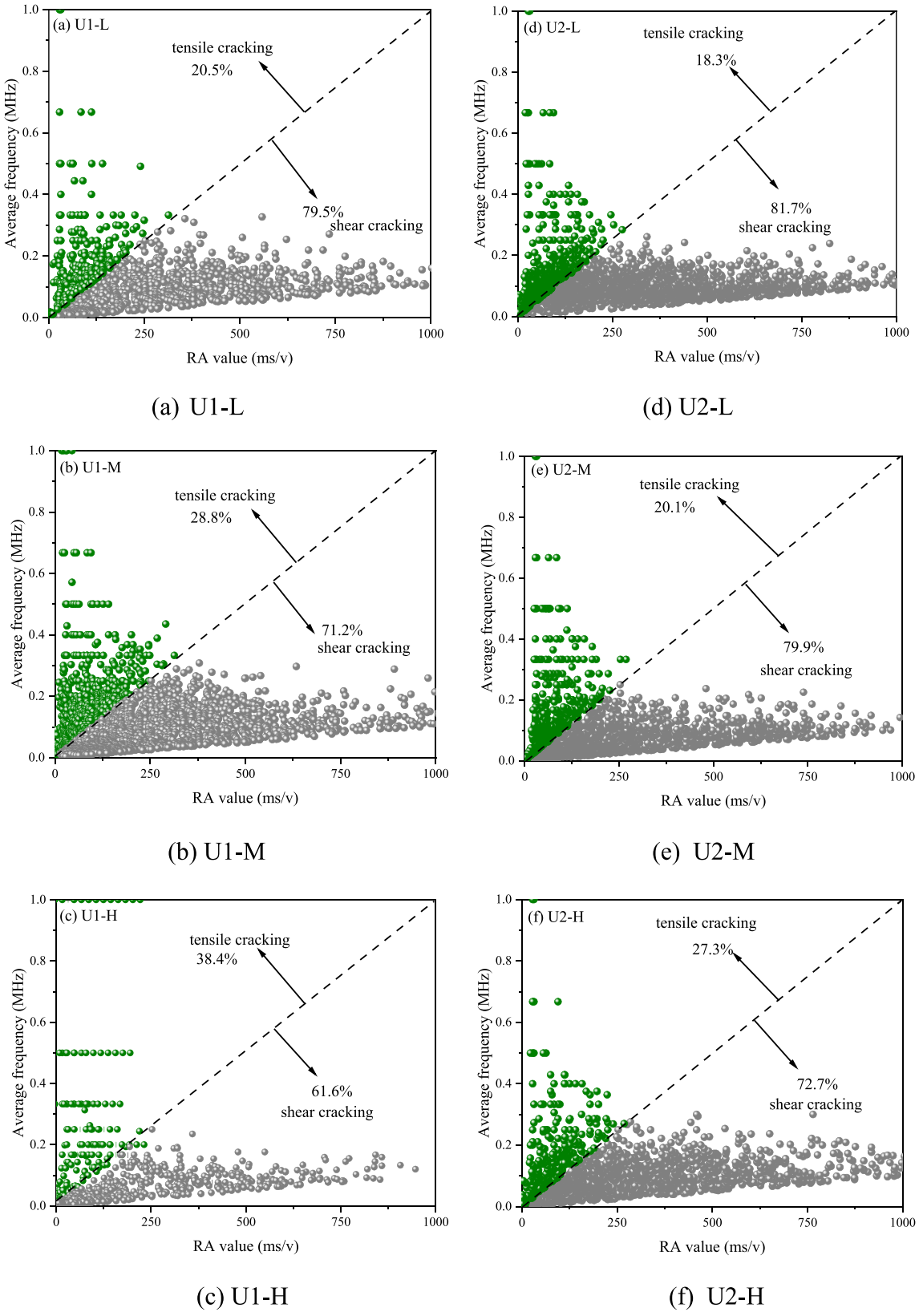

Fig. 9. Average frequency versus RA value for the corroded UHPFRC.

microscopic images demonstrate that the propagation of matrix crack, dissolution and splitting of steel fiber induce a further increased deterioration of UHPFRC with the increase of fiber contents and corrosion time.

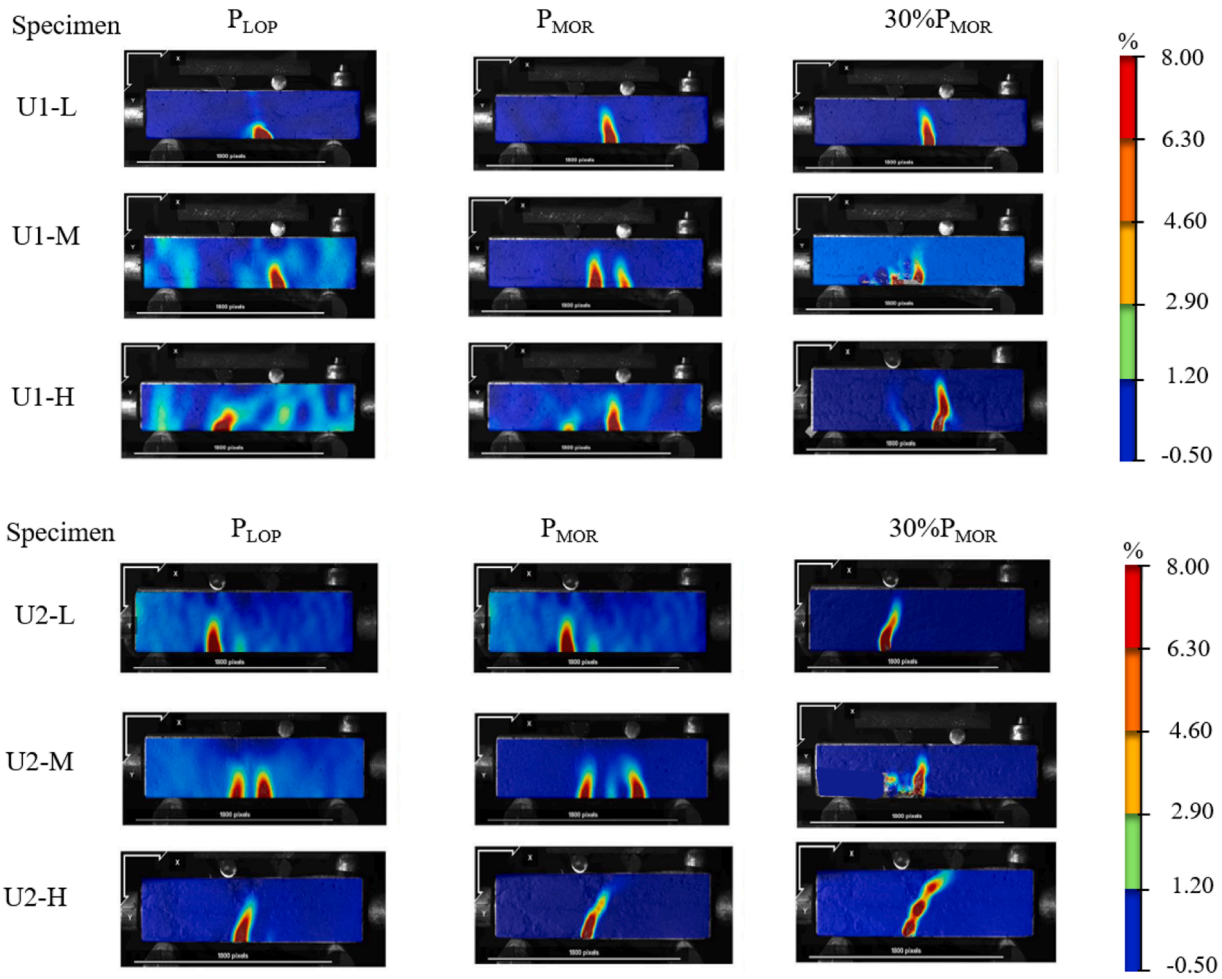

Fig. 10. Strain field in corroded specimens during the four-point flexural test.

4. Discussion

4.1. Chemical reaction and microstructure change of UHPFRC in aggressive environment

Corrosion of UHPFRC is easy to be ignored and difficult to be characterized considering the condition of unevenly dispersed fibers in the matrix and its dense structure. But steel fiber in UHPFRC is inevitably corroded when UHPFRC is exposed to a chloride-containing erosion environment.

The nature of steel fiber drives UHPFRC specimens to corrode and deteriorate under an aggressive environment [9,21]. As shown in Fig. 13, steel fiber corrosion and matrix deterioration are mainly caused by the continuous invasion of chloride ions and the leaching of calcium in the matrix. When UHPFRC serves in an aggressive environment, calcium hydroxide and C-S-H gel are continuously leached through the pore solution under the action of internal and external concentration differences between liquid and solid environment, increasing the porosity of the matrix and ultimately reducing the mechanical strength of the matrix [9,21,58–60]. In our previous paper [9], fiber corrosion causes a decrease in the mechanical strength of the surrounding matrix as measured by the nanoindentation technique. Similarly, the MIP analysis in our another study [21] also show that fiber corrosion increased the porosity of the matrix. When steel fibers as a toughened material in UHPFRC are subjected to corrosion, they would always be accompanied by a series of adverse effects including the peeling of concrete cover, rust or even fracture of steel fibers and cracking of surrounding matrix, etc. [9,12,21,61]. Due to its high conductivity and interface porosity, UHPFRC with high fiber contents gets a greater corrosion risk [62,63]. Also, the large weak interfaces between fibers and matrix provide preferential paths for chloride ingress [9]. Over corrosion time, chloride accumulates on the fiber surface which destroys the passive layer of steel fiber and makes the fiber corrode. Meanwhile, calcium leaching will also increase the porosity of the matrix, leading to a more rapid diffusion of chloride ions through the concrete. Thus, steel fibers expand and spilt to different degrees with the increased corrosion (Fig. 11), and interface degradation is also obvious with the increased corrosion damage, showing matrix cracking, fiber splitting and other degradation phenomena (Fig. 12). As a result, UHPFRC structures undergo continuous deterioration due to the combination of fiber corrosion and matrix degradation caused by chloride ingress and calcium leaching. When UHPFRC suffers from corrosion, the steel fibers near the matrix cover are the first to undergo an oxidation reaction, which would inevitably induce fiber swelling and concrete cracking with the increased corrosion damage. The aggressive solution constantly erodes the matrix, resulting in the degradation of the surrounding matrix (Fig. 4).

4.2. The fracture evolution process of corroded UHPFRC during bending behavior

Previous studies have reported that the analysis combined with AE and DIC can effectively characterize the cracking behavior and strain field of concrete [4,28,31,44,52,64,65]. This chapter aims to discuss the fracture process of corroded UHPFRC by integrating the results acquired from AE events and the DIC technique.

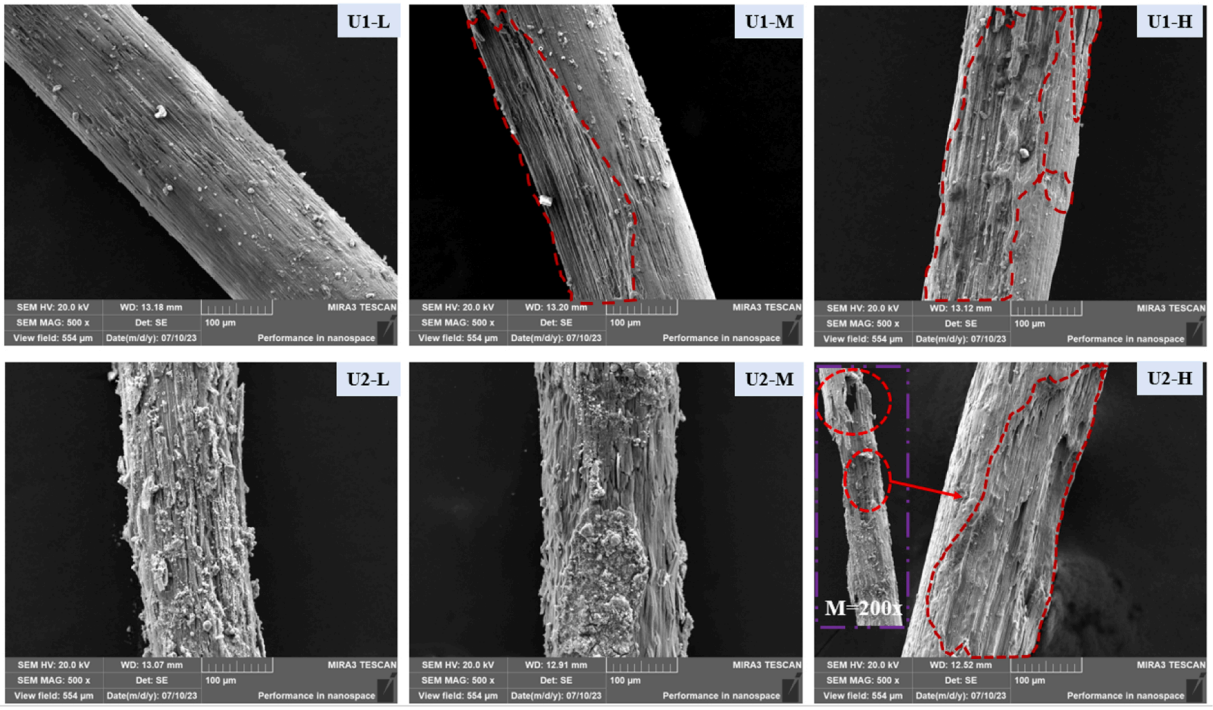

Fig. 11. Surface morphology of the representative steel fiber from the corroded UHPFRC specimen with various corrosion degree by BSE imaging (Magnification = 500, 200 X).

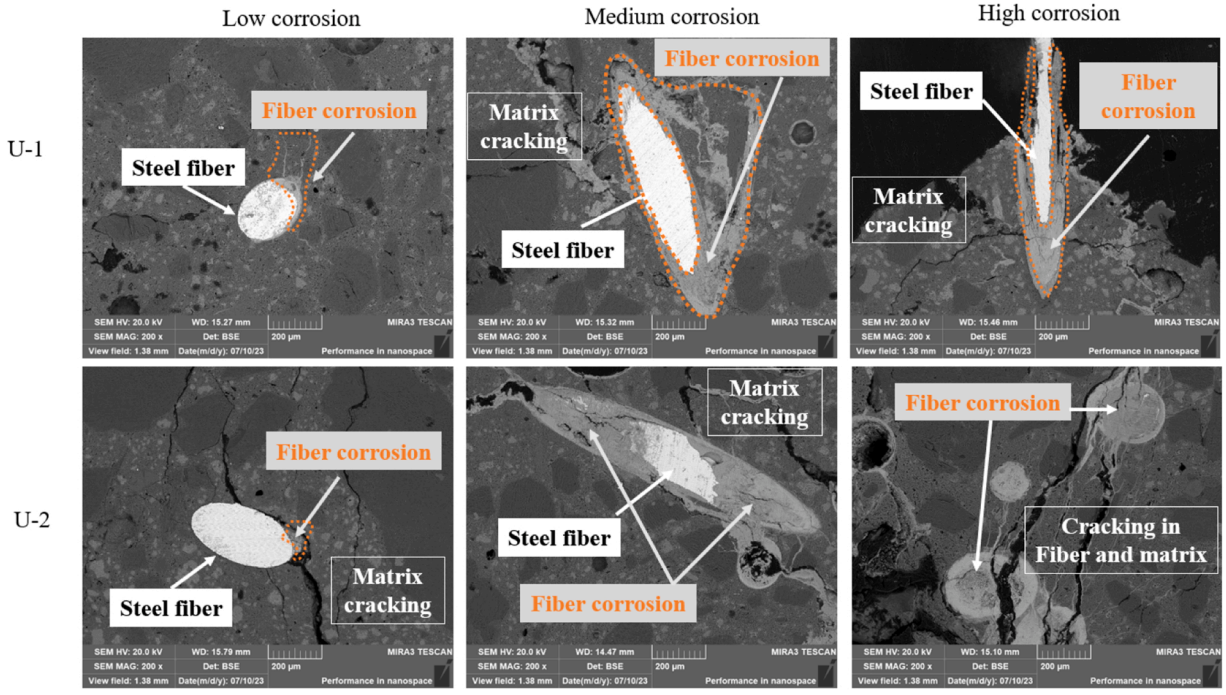

Fig. 12. Cross-sectional images of the corroded steel fiber on UHPFRC upon different corrosion degree (Magnification = 200 X).

The failure pattern is an important response of the corroded UHPFRC under loading, which has a close relationship with strength and energy absorption. During crack initiation, AE energy is emitted in the form of elastic waves that propagate from the crack location to the surface of the specimen [65,66]. Fig. 14 shows the AE hit distribution diagram together with the load-time curve, where the factor of corrosion degree is considered. The bending failure of UHPFRC can be assigned to the cracking of concrete matrix, failure of corroded fiber, bridge of the non-corroded fiber, fiber-matrix debonding, steel fiber pullout or fracture. For example, with the increase in corrosion degree, U2-L shows a higher cracking load and acoustic emission vibration than the other heavy corroded specimens of U2-M and U2-H (Fig. 14). This is because, at low corrosion damage, the steel fiber corrosion is not serious and the cover matrix is still relatively dense. The matrix is not subjected to serious calcium leaching and is not influenced by the expansion and extrusion of the corrosion product. Thus, the matrix strength is high and

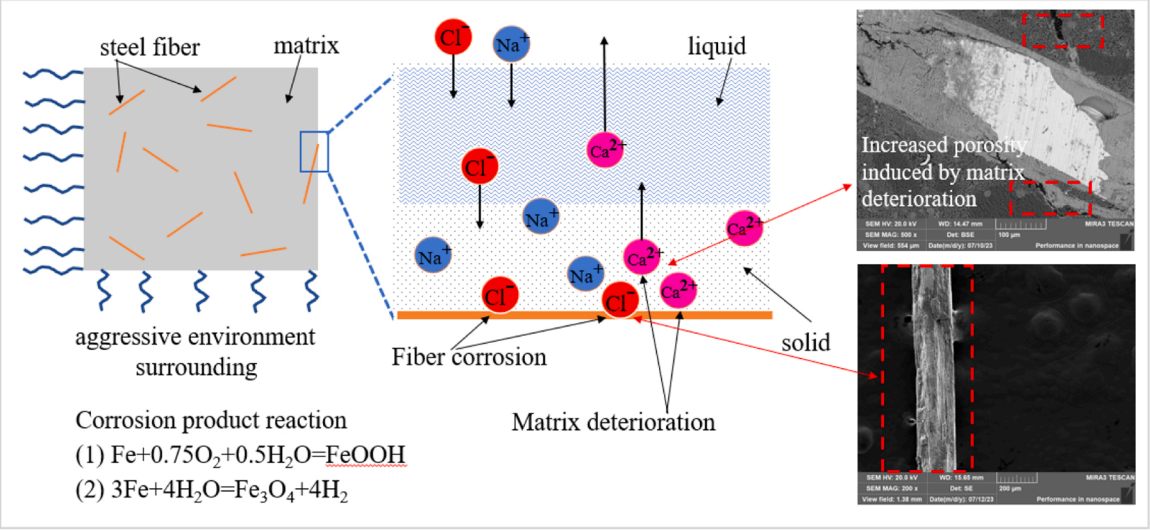

Fig. 13. Schematic diagram of steel fiber corrosion and matrix deterioration in UHPFRC under an aggressive environment considering chloride ingress.

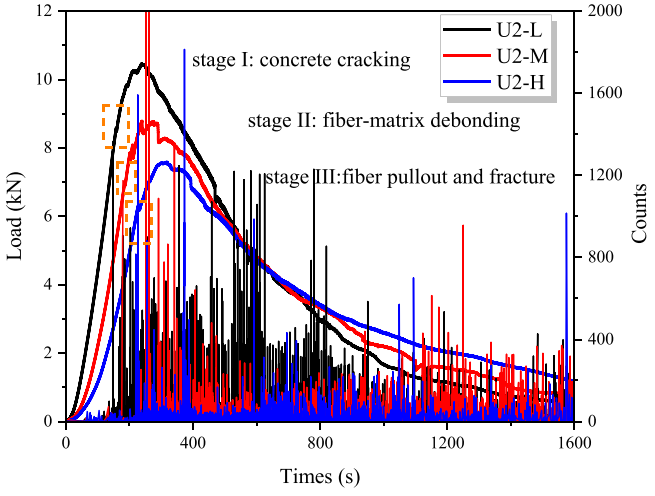

Fig. 14. AE hit distribution diagram together with load-time curve considering the influence factor of corrosion degree.

the bond between the steel fiber and the matrix is still dense, leading to a high cracking point. During stage II of the points between concrete cracking and peak loading, AE hit distribution decreases obviously with the increase of corrosion damage due to the loose fiber-matrix interface influenced by fiber corrosion (Fig. 14). But there are still a large number of uncorroded steel fibers inside that show a well-bonded capacity with matrix together in consistent denaturation. The undamaged fiber would redistribute stress, adjust the microstructural stress skeleton, and further develop the potential mechanical capabilities. During the unloading stage, the signals of fiber pullout and fracture decrease obviously with the increase of corrosion damage (Fig. 14), showing a high ductility in U2-L.

The failure pattern of UHPFRC specimens without corrosion damage under quasi-static conditions is mainly controlled by the pull-out of steel fibers [3], but the fracture mechanism of UHPFRC exposed to different corrosion damage is rarely characterized. The fracture evolution process of corroded UHPFRC specimens is different from that of conventional UHPFRC, considering that steel fiber corrosion will lead to different degrees of deterioration of steel fibers themselves, the interface of fiber-matrix and the matrix itself. The macroscopic damage of a material like corroded UHPFRC is the manifestation of its internal micro-structure damage evolution [64,67]. The failure mechanism of the UHPFRC exposed to various corrosion damage is illustrated in Fig. 15. In this work, for the low corrosion damage, after the cracks go through the small deteriorated zones of the matrix, the external stress can still be dispersed from the good matrix through the internal undamaged steel fiber (Fig. 15 (a)). The undamaged steel fibers with a three-dimensional distribution in the matrix effectively limit the expansion and coalescence of cracks, change the direction of cracks, and finally maintain the bearing capacity of the slight corroded UHPFRC. UHPFRC specimen with low corrosion damage exhibits a higher AE signal (Fig. 7) and the proportion of shear cracks up to 79.5% (Fig. 9), which is attributed to the pullout of inside non-corroded fiber. Damage area of the surrounding cover in UHPFRC is larger with the increased corrosion invasion (Fig. 15 (b, c)) [20]. For the heavy corroded UHPFRC specimens, the deteriorated matrix and steel fiber are too weak to deliver the loading stress and therefore rupture occurs [37]. With the increase of corrosion damage, cracks would seek relatively weaker regions, more cracks crush the deteriorated zones e.g., loose matrix, corroded steel fibers, deteriorated interface of fiber-matrix. Multiple cracks are generated in the deteriorated zones at higher corrosion damage so that the deteriorated corrosion zones bear more stress before the cracks have enough time to seek the weaker regions in the small undeteriorated zones. The load stress quickly breaks the weak area, showing the reduction in the AE signals and a higher strain in the crack (Fig. 7 ~ 10), making an obvious increase of tensile cracks of U1-H (38.4%) up to 87.3% than that of U1-L (20.5%). The degradation phenomena e.g., initiation and expansion of micro-crack in the microstructure, are external appearances during the process of concrete damage evolution.

As abovementioned, fracture process of the corroded UHPFRC specimen involves the deformation of matrix, interfacial extrusion of fiber-matrix and pullout or fracture of steel fiber during the flexural action. Cracks begin to spread primarily along the weak interface of the corroded steel fiber and matrix, and even through the corroded steel fiber itself. After primary crack generates, the steel fiber in the deep layer without serious corrosion would be accompanied with elastic-plastic deformation, fiber debonding and fiber slippage, controlling the main bearing capacity. However, for the heavily corroded UHPFRC with bigger deteriorated zones, the strength of matrix and interface of fiber-matrix is significantly reduced compared with the slightly corroded UHPFRC. Cracking around the large weak zone becomes the main failure pattern due to that the cracks have no time to reach the undamaged zones, which shows differences from slight corroded

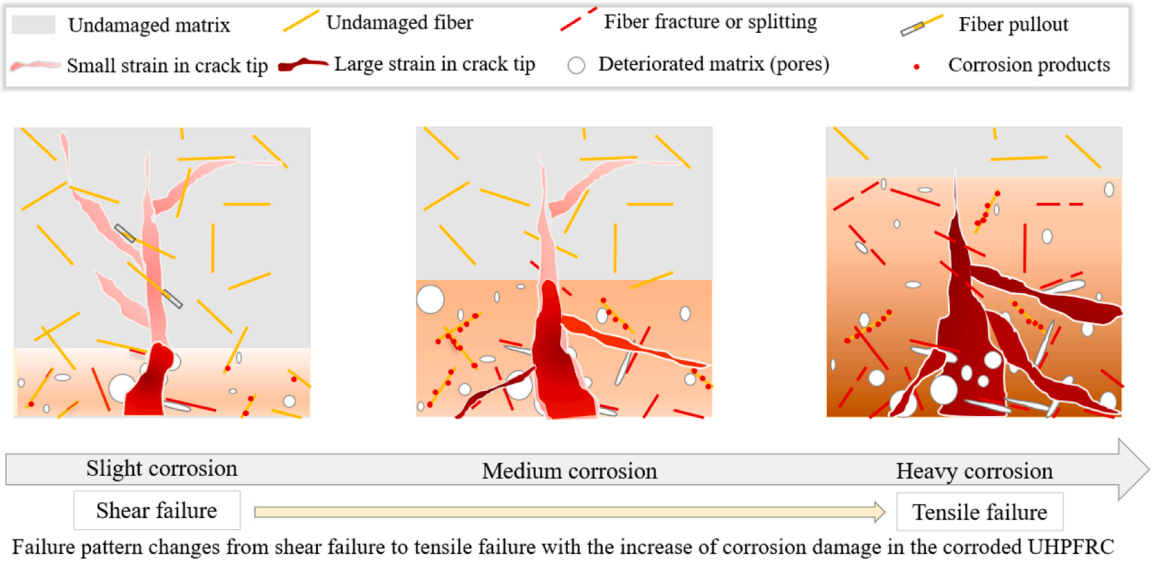

Fig. 15. Schematic diagram of cracking performance on the corroded UHPFRC under the four-point flexural loading.

UHPFRC. As a result, the presence of fiber corrosion and matrix deterioration leads to significant decreases in the mechanical strength and energy consumption. Failure patterns change from a typical shear failure to tensile failure as the corrosion damage increases, which sheds light on the fracture evolution process of the UHPFRC with various corrosion degrees.

There are very limited studies on the fracture mechanism of corroded UHPFRC. The obtained results can correspond to different stages of deterioration conditions in real projects, respectively. This is a very encouraging result towards the quantitative assessment of microfracture characteristics of corroded UHPFRC based on the correlation between DIC and AE measurements for real-world structures. The durability and damage mechanism of concrete under the action of a single factor is the basis for studying the multiple factors that influence the durability and damage mechanism of concrete. Thus, this paper carries out an in-depth study of the fracture mechanism of corroded UHPFRC. The corrosion-induced deterioration and fracture pattern of the durability performance of corroded UHPFRC is revealed by combining the microfine analysis of the material and the macroscopic fracture properties. It has to be admitted that the factors affecting the durability of UHPFRC are complex, and the research scope is wide. The study of the durability deterioration mechanism of UHPFRC under the joint action of multiple factors is even long-term and arduous work. This work provides a reference for the corrosion monitoring of UHPFRC during service life and enriches the research scope of UHPFRC. By elucidating the transformation of the fracture mechanism of the UHPFRC with various corrosion, this work provides experimental data as a reference for future numerical simulation and prediction.

5. Conclusions

This study investigates the fracture evolution and detection of micro/macro-cracking in corroded UHPFRC using a combination of AE and DIC techniques. 3D laser scanning is employed to reproduce the corroded specimen. SEM is used to observe fiber swelling and interface cracking. As for crack classification in corroded UHPFRC by AE technique, the transition of failure pattern is for the first time proposed according to different corrosion degrees. Moreover, the relationships between the AE events and energies-duration are investigated to verify the fracture evolution of the integrated AE signal and DIC strain. Two conceptual models of corrosion-induced deterioration and fracture mechanism of the UHPFRC upon corrosion are proposed. The main conclusions can be drawn:

(1) Corroded UHPFRC specimens have an obvious surface deterioration with the increase of steel fiber content and corrosion duration. The 56-day weight loss of corroded UHPFRC with 2 vol % develops up to 6.1%.

(1) An increase in the corrosion duration and fiber contents yields a decrease in mechanical properties. The flexural strength of U1 declines up to 28% with the increasing corrosion damage. The specimen with 2 vol% being subjected to 56-day corrosion duration is found to be the most severe among the investigated series, showing a reduction in compressive strength and flexural stiffness up to 29.1% and 31.6%. The toughness ($T_{2.4}$) of U2-H loses 27.5% compared to the specimen with low corrosion damage, while the value is up to 37% for the U1.
(2) The proportion of the AE counts and shear crack of the corroded UHPFRC reduces with the increase of corrosion damage. Failure mode changes from shear failure to a brittle failure of tensile crack as corrosion damage increases.
(3) The strain field in the deteriorated zones of the corroded UHPFRC increases with the increase of corrosion deterioration. Fiber corrosion facilitates the generation of initial defects, leading to the rapid spread of cracks through the deteriorated area at the bottom to the upper, showing a high strain value up to 0.8 at the specimen with 2 vol% being subjected to 56-day corrosion duration.
(4) The stress rapidly passes through the deteriorated matrix and steel fibers of UHPFRC. The stress at the crack tip would purposefully develop towards the matrix and steel fibers without damage, playing an important role in internal force redistribution, adjusting the microstructural stress skeleton and further developing the potential bearing capabilities.

The obtained results in this research can correspond to different stages of deterioration conditions in real projects, respectively. The initial corrosion time of steel fibers and the initial crack time of concrete are important factors affecting the structural design and durability of UHPFRC structures. This work provides experimental data as a reference for future numerical simulation, life prediction, detection and repair of corroded UHPFRC. Further exploration with more attempt at characterization analysis and fiber corrosion is necessary. More external

factors of loading rates and environmental parameters might influence the fracture patterns.

CRediT authorship contribution statement

Zhaoping Song: Methodology, Investigation, Data analysis, Validation, Writing – original draft. **Shaohua Li:** Data analysis, Writing – review & editing. **Lulu Cheng:** Writing – review & editing. **Qingliang Yu:** Conceptualization, Methodology, Supervision, Funding acquisition, Project administration, Writing – review & editing.

Declaration of Competing Interest

The authors declare that they have no known competing financial interests or personal relationships that could have appeared to influence the work reported in this paper.

Data availability

Data will be made available on request.

Acknowledgments

This work was financially supported by the National Natural Science Foundation of China (Grant No. 52178246; 52374223; 52308414); and Hubei Province Key research and development plan (Grant No. 2023BAB105).

References

[1] A.M. Matos, S. Chaves Figueiredo, S. Nunes, E. Schlangen, J.L. Barroso-Aguiar, Durability of an UHPFRC under mechanical and chloride loads, Constr. Build. Mater. 311 (2021), https://doi.org/10.1016/j.conbuildmat.2021.125223.
[2] N. Schramm, O. Fischer, Precast bridge construction with UHPFRC—Shear tests and railway bridge pilot application, Civ. Eng. Des. 1 (2019) 41–53, https://doi.org/10.1002/cend.201800005.
[3] Q. Yu, W. Zhuang, C. Shi, Research progress on the dynamic compressive properties of ultra-high performance concrete under high strain rates, Cem. Concr. Compos. 124 (2021) 104258, https://doi.org/10.1016/j.cemconcomp.2021.104258.
[4] Q. Zheng, C. Li, B. He, Z. Jiang, Revealing the effect of silica fume on the flexural behavior of ultra-high-performance fiber-reinforced concrete by acoustic emission technique, Cem. Concr. Compos. 131 (2022) 104563, https://doi.org/10.1016/j.cemconcomp.2022.104563.
[5] M. Gesoglu, E. Güneyisi, G.F. Muhyaddin, D.S. Asaad, Strain hardening ultra-high performance fiber reinforced cementitious composites: Effect of fiber type and concentration, Compos. Part B Eng. 103 (2016) 74–83, https://doi.org/10.1016/j.compositesb.2016.08.004.
[6] D. Wang, C. Shi, Z. Wu, J. Xiao, Z. Huang, Z. Fang, A review on ultra high performance concrete: Part II. Hydration, microstructure and properties, Constr. Build. Mater. 96 (2015) 368–377, https://doi.org/10.1016/j.conbuildmat.2015.08.095.
[7] Y.Y.Y. Cao, Q.H. Tan, Z.G. Jiang, H.J.H. Brouwers, Q.L. Yu, A nonlinear rate-dependent model for predicting the depth of penetration in ultra-high performance fiber reinforced concrete (UHPFRC), Cem. Concr. Compos. 106 (2020), https://doi.org/10.1016/j.cemconcomp.2019.103451.
[8] J. Provete Vincler, T. Sanchez, V. Turgeon, D. Conciatori, L. Sorelli, A modified accelerated chloride migration tests for UHPC and UHPFRC with PVA and steel fibers, Cem. Concr. Res. 117 (2019) 38–44, https://doi.org/10.1016/j.cemconres.2018.12.006.
[9] Z. Song, S. Li, Q. Yu, Chloride induced mechanical degradation of ultra-high performance fiber-reinforced concrete: Insights from corrosion evolution paths, Constr. Build. Mater. 395 (2023) 132329, https://doi.org/10.1016/j.conbuildmat.2023.132329.
[10] S. Zhang, D. Gao, H. Zhu, L. Chen, Z. He, L. Yang, Flexural behavior of seawater-mixed steel fiber reinforced concrete exposed to simulated marine environments, Constr. Build. Mater. 373 (2023) 130858, https://doi.org/10.1016/j.conbuildmat.2023.130858.
[11] Q. Song, R. Yu, Z. Shui, S. Rao, X. Wang, M. Sun, C. Jiang, Steel fibre content and interconnection induced electrochemical corrosion of Ultra-High Performance Fibre Reinforced Concrete (UHPFRC), Cem. Concr. Compos. 94 (2018) 191–200, https://doi.org/10.1016/j.cemconcomp.2018.09.010.
[12] L.S. Lv, J.Y. Wang, R.C. Xiao, M.S. Fang, Y. Tan, Influence of steel fiber corrosion on tensile properties and cracking mechanism of ultra-high performance concrete in an electrochemical corrosion environment, Constr. Build. Mater. 278 (2021) 122338, https://doi.org/10.1016/j.conbuildmat.2021.122338.
[13] D.Y. Yoo, W. Shin, B. Chun, N. Banthia, Assessment of steel fiber corrosion in self-healed ultra-high-performance fiber-reinforced concrete and its effect on tensile performance, Cem. Concr. Res. 133 (2020), https://doi.org/10.1016/j.cemconres.2020.106091.
[14] D.Y. Yoo, W. Shin, B. Chun, Corrosion effect on tensile behavior of ultra-high-performance concrete reinforced with straight steel fibers, Cem. Concr. Compos. 109 (2020) 103566, https://doi.org/10.1016/j.cemconcomp.2020.103566.
[15] J.Y. Wang, J.Y. Guo, Damage investigation of ultra high performance concrete under direct tensile test using acoustic emission techniques, Cem. Concr. Compos. 88 (2018) 17–28, https://doi.org/10.1016/j.cemconcomp.2018.01.007.
[16] Y.S. Jang, D.Y. Yoo, Combined chelating and corrosion effects of steel fiber on the interfacial bond and tensile behaviors of ultra-high-performance concrete, Cem. Concr. Compos. 129 (2022) 104505, https://doi.org/10.1016/j.cemconcomp.2022.104505.
[17] S. Pyo, T. Koh, M. Tafesse, H.K. Kim, Chloride-induced corrosion of steel fiber near the surface of ultra-high performance concrete and its effect on flexural behavior with various thickness, Constr. Build. Mater. 224 (2019) 206–213, https://doi.org/10.1016/j.conbuildmat.2019.07.063.
[18] W. Shin, D.Y. Yoo, Influence of steel fibers corroded through multiple microcracks on the tensile behavior of ultra-high-performance concrete, Constr. Build. Mater. 259 (2020) 120428, https://doi.org/10.1016/j.conbuildmat.2020.120428.
[19] K. Hashimoto, T. Toyoda, H. Yokota, K. Kono, T. Kawaguchi, Tension-softening behavior and chloride ion diffusivity of cracked ultra high strength fiber reinforced concrete, RILEM-Fib-AFGC Int. Symp. Ultra-High. Perform. Fibre-Reinf. Concr. UHPFRC 2013 (2013) 257–264.
[20] L. Fan, W. Meng, L. Teng, K.H. Khayat, Effect of steel fibers with galvanized coatings on corrosion of steel bars embedded in UHPC, Compos. Part B Eng. 177 (2019) 107445, https://doi.org/10.1016/j.compositesb.2019.107445.
[21] Z. Song, S. Li, H.J.H. Brouwers, Q. Yu, Corrosion risk and corrosion-induced deterioration of ultra-high performance fiber-reinforced concrete containing initial micro-defects, Cem. Concr. Compos. 142 (2023) 105208, https://doi.org/10.1016/j.cemconcomp.2023.105208.
[22] Y. Zhou, X. Yu, Z. Guo, Y. Yan, K. Zhao, J. Wang, S. Zhu, On acoustic emission characteristics, initiation crack intensity, and damage evolution of cement-paste backfill under uniaxial compression, Constr. Build. Mater. 269 (2021) 121261, https://doi.org/10.1016/j.conbuildmat.2020.121261.
[23] Y. Niu, H. Huang, J. Zhang, W. Jin, J. Wei, Q. Yu, Development of the strain field along the crack in ultra-high-performance fiber-reinforced concrete (UHPFRC) under bending by digital image correlation technique, Cem. Concr. Res. 125 (2019) 105821, https://doi.org/10.1016/j.cemconres.2019.105821.
[24] B. Mobasher, A. Li, Y. Yao, A. Arora, N. Neithalath, Characterization of toughening mechanisms in UHPC through image correlation and inverse analysis of flexural results, Cem. Concr. Compos. 122 (2021) 104157, https://doi.org/10.1016/j.cemconcomp.2021.104157.
[25] L. Weng, Z. Wu, Q. Liu, Influence of heating/cooling cycles on the micro/macrocracking characteristics of Rucheng granite under unconfined compression, Bull. Eng. Geol. Environ. 79 (2020) 1289–1309, https://doi.org/10.1007/s10064-019-01638-4.
[26] X. Shen, E. Brühwiler, Influence of local fiber distribution on tensile behavior of strain hardening UHPFRC using NDT and DIC, Cem. Concr. Res. 132 (2020) 106042, https://doi.org/10.1016/j.cemconres.2020.106042.
[27] P. Aghdasi, C.P. Ostertag, Tensile fracture characteristics of Green Ultra-High Performance Fiber-Reinforced Concrete (G-UHP-FRC) with longitudinal steel reinforcement, Cem. Concr. Compos. 114 (2020) 103749, https://doi.org/10.1016/j.cemconcomp.2020.103749.
[28] K. Pan, R.C. Yu, G. Ruiz, X. Zhang, Z. Wu, Á. De La Rosa, The propagation speed of multiple dynamic cracks in fiber-reinforced cement-based composites measured using DIC, Cem. Concr. Compos. 122 (2021) 104140, https://doi.org/10.1016/j.cemconcomp.2021.104140.
[29] K. Hannawi, H. Bian, W. Prince-Agbodjan, B. Raghavan, Effect of different types of fibers on the microstructure and the mechanical behavior of Ultra-High Performance Fiber-Reinforced Concretes, Compos. Part B Eng. 86 (2016) 214–220, https://doi.org/10.1016/j.compositesb.2015.09.059.
[30] S. Granger, A. Loukili, G. Pijaudier-Cabot, G. Chanvillard, Experimental characterization of the self-healing of cracks in an ultra high performance cementitious material: mechanical tests and acoustic emission analysis, Cem. Concr. Res. 37 (2007) 519–527, https://doi.org/10.1016/j.cemconres.2006.12.005.
[31] S.C. Paul, S. Pirskawetz, G.P.A.G. Van Zijl, W. Schmidt, Acoustic emission for characterising the crack propagation in strain-hardening cement-based composites (SHCC), Cem. Concr. Res. 69 (2015) 19–24, https://doi.org/10.1016/j.cemconres.2014.12.003.
[32] W. Zhuang, S. Li, Z. Wang, Z. Zhang, Q. Yu, Impact of micromechanics on dynamic compressive behavior of ultra-high performance concrete containing limestone powder, Compos. Part B Eng. 243 (2022) 110160, https://doi.org/10.1016/j.compositesb.2022.110160.
[33] H.J.H. Brouwers, H.J. Radix, Self-compacting concrete: theoretical and experimental study, Cem. Concr. Res. 35 (2005) 2116–2136, https://doi.org/10.1016/j.cemconres.2005.06.002.
[34] Q.L. Yu, H.J.H. Brouwers, Development of a self-compacting gypsum-based lightweight composite, Cem. Concr. Compos. 34 (2012) 1033–1043, https://doi.org/10.1016/j.cemconcomp.2012.05.004.
[35] Q.L. Yu, P. Spiesz, H.J.H. Brouwers, Development of cement-based lightweight composites - Part 1: mix design methodology and hardened properties, Cem. Concr. Compos. 44 (2013) 17–29, https://doi.org/10.1016/j.cemconcomp.2013.03.030.

[36] G. Benjamin, A., Material property characterization of ultra-high performance concrete, Fhwa (2006) 186.
[37] W. Xu, Y. Li, H. Li, K. Wang, C. Zhang, Y. Jiang, S. Qiang, Corrosion mechanism and damage characteristic of steel fiber concrete under the effect of stray current and salt solution, Constr. Build. Mater. 314 (2022), https://doi.org/10.1016/j.conbuildmat.2021.125618.
[38] L. Zhang, Z. Liang, S. Li, Effect of current density on the cathodic protection efficiency and mechanical properties of pre-stressed high-strength steel wires for stay cable, Constr. Build. Mater. 314 (2022) 125671, https://doi.org/10.1016/j.conbuildmat.2021.125671.
[39] G.S. Duffó, S.B. Farina, F.M.S. Rodríguez, Corrosion behaviour of non-ferrous metals embedded in mortar, Constr. Build. Mater. 210 (2019) 548–554, https://doi.org/10.1016/j.conbuildmat.2019.03.208.
[40] G. Chen, M.N.S. Hadi, D. Gao, L. Zhao, Experimental study on the properties of corroded steel fibres, Constr. Build. Mater. 79 (2015) 165–172, https://doi.org/10.1016/j.conbuildmat.2014.12.082.
[41] L. Hou, Y. Peng, R. Xu, X. Zhang, T. Huang, D. Chen, Corrosion behavior and flexural performance of reinforced SFRC beams under sustained loading and chloride attack, Eng. Struct. 242 (2021) 112553, https://doi.org/10.1016/j.engstruct.2021.112553.
[42] Y. Song, K. Li, W. Tian, Mechanical response of sandstone exposed to monotonic and multilevel fatigue loading: Insights from deformation, energy and acoustic emission characteristics, Theor. Appl. Fract. Mech. (2023) 104181, https://doi.org/10.1016/j.tafmec.2023.104181.
[43] W. Li, Z. Jiang, Q. Yu, Multiple damaging and self-healing properties of cement paste incorporating microcapsules, Constr. Build. Mater. 255 (2020) 119302, https://doi.org/10.1016/j.conbuildmat.2020.119302.
[44] J.G. Yue, Y.N. Wang, D.E. Beskos, Uniaxial tension damage mechanics of steel fiber reinforced concrete using acoustic emission and machine learning crack mode classification, Cem. Concr. Compos. 123 (2021) 104205, https://doi.org/10.1016/j.cemconcomp.2021.104205.
[45] W. Conshohocken, Stand. Test. Method Meas. Initiat. Toughness Surf. Cracks Tens. Bend. 1 (2014) 1–39, https://doi.org/10.1520/E2899-13.2.
[46] M. Ohtsu, T. Isoda, Y. Tomoda, Acoustic emission techniques standardized for concrete structures, J. Acoust. Emiss. 25 (2007) 21.
[47] Z. Chen, G. Zhang, R. He, Z. Tian, C. Fu, X. Jin, Acoustic emission analysis of crack type identification of corroded concrete columns under eccentric loading: a comparative analysis of RA-AF method and Gaussian mixture model, Case Stud. Constr. Mater. 18 (2023) e02021, https://doi.org/10.1016/j.cscm.2023.e02021.
[48] Y. Farnam, M.R. Geiker, D. Bentz, J. Weiss, Acoustic emission waveform characterization of crack origin and mode in fractured and ASR damaged concrete, Cem. Concr. Compos. 60 (2015) 135–145, https://doi.org/10.1016/j.cemconcomp.2015.04.008.
[49] J. Xu, J.D. Houndehou, Z. Wang, Q. Ma, Experimental investigation on the mechanical properties and damage evolution of steel-fiber-reinforced crumb rubber concrete with porcelain tile waste, Constr. Build. Mater. 370 (2023) 130643, https://doi.org/10.1016/j.conbuildmat.2023.130643.
[50] D.G. Aggelis, D.V. Soulioti, N.M. Barkoula, A.S. Paipetis, T.E. Matikas, Influence of fiber chemical coating on the acoustic emission behavior of steel fiber reinforced concrete, Cem. Concr. Compos. 34 (2012) 62–67, https://doi.org/10.1016/j.cemconcomp.2011.07.003.
[51] B. Li, L. Xu, Y. Shi, Y. Chi, Q. Liu, C. Li, Effects of fiber type, volume fraction and aspect ratio on the flexural and acoustic emission behaviors of steel fiber reinforced concrete, Constr. Build. Mater. 181 (2018) 474–486, https://doi.org/10.1016/j.conbuildmat.2018.06.065.
[52] I. Saha, R. Vidya Sagar, Classification of the acoustic emissions generated during the tensile fracture process in steel fibre reinforced concrete using a waveform-based clustering method, Constr. Build. Mater. 294 (2021) 123541, https://doi.org/10.1016/j.conbuildmat.2021.123541.
[53] Q. Song, R. Yu, Z. Shui, L. Chen, Z. Liu, X. Gao, J. Zhang, Y. He, Intrinsic effect of hybrid fibres 3D network on the electrochemical characteristics of Ultra-High Performance Fibre Reinforced Composites (UHPFRC), Cem. Concr. Compos. 114 (2020) 103818, https://doi.org/10.1016/j.cemconcomp.2020.103818.
[54] Z. Li, Z. Jin, Y. Gao, T. Zhao, P. Wang, Z. Li, Coupled application of innovative electromagnetic sensors and digital image correlation technique to monitor corrosion process of reinforced bars in concrete, Cem. Concr. Compos. 113 (2020) 103730, https://doi.org/10.1016/j.cemconcomp.2020.103730.
[55] W. Xu, Y. Li, H. Li, K. Wang, C. Zhang, Y. Jiang, S. Qiang, Corrosion mechanism and damage characteristic of steel fiber concrete under the effect of stray current and salt solution, Constr. Build. Mater. 314 (2022), https://doi.org/10.1016/j.conbuildmat.2021.125618.
[56] K.L. Scrivener, A.K. Crumbie, P. Laugesen, The interfacial transition zone (ITZ) between cement paste and aggregate in concrete, Interface Sci. 12 (2004) 411–421, https://doi.org/10.1023/B:INTS.0000042339.92990.4c.
[57] R. Yu, P. Spiesz, H.J.H. Brouwers, Mix design and properties assessment of ultra-high performance fibre reinforced concrete (UHPFRC), Cem. Concr. Res. 56 (2014) 29–39, https://doi.org/10.1016/j.cemconres.2013.11.002.
[58] Q. feng Liu, X. han Shen, B. Šavija, Z. Meng, D.C.W. Tsang, S. Sepasgozar, E. Schlangen, Numerical study of interactive ingress of calcium leaching, chloride transport and multi-ions coupling in concrete, Cem. Concr. Res. 165 (2023), https://doi.org/10.1016/j.cemconres.2022.107072.
[59] Z. Song, Y. Liu, L. Jiang, M. Guo, J. Chen, W. Wang, N. Xu, Determination of calcium leaching behavior of cement pastes exposed to ammonium chloride aqueous solution via an electrochemical impedance spectroscopic approach, Constr. Build. Mater. 196 (2019) 267–276, https://doi.org/10.1016/j.conbuildmat.2018.11.128.
[60] X. Wang, K. Xu, Y. Li, S. Guo, Dissolution and leaching mechanisms of calcium ions in cement based materials, Constr. Build. Mater. 180 (2018) 103–108, https://doi.org/10.1016/j.conbuildmat.2018.05.225.
[61] B. Šavija, M. Luković, S.A.S. Hosseini, J. Pacheco, E. Schlangen, Corrosion induced cover cracking studied by X-ray computed tomography, nanoindentation, and energy dispersive X-ray spectrometry (EDS), Mater. Struct. Constr. 48 (2015) 2043–2062, https://doi.org/10.1617/s11527-014-0292-9.
[62] J. Han, Z. Miao, J. Wang, X. Zhang, Y. Lv, Investigation of the corrosion-induced damage mechanism of steel fibers in ultra-high-performance steel fiber-reinforced concrete using X-ray computed tomography, Constr. Build. Mater. 368 (2023) 130429, https://doi.org/10.1016/j.conbuildmat.2023.130429.
[63] L. Fan, W. Meng, L. Teng, K.H. Khayat, Effects of lightweight sand and steel fiber contents on the corrosion performance of steel rebar embedded in UHPC, Constr. Build. Mater. 238 (2020) 117709, https://doi.org/10.1016/j.conbuildmat.2019.117709.
[64] H. Zhang, C. Jin, L. Wang, L. Pan, X. Liu, S. Ji, Research on dynamic splitting damage characteristics and constitutive model of basalt fiber reinforced concrete based on acoustic emission, Constr. Build. Mater. 319 (2022) 126018, https://doi.org/10.1016/j.conbuildmat.2021.126018.
[65] S. Ashraf, M. Rucka, Microcrack monitoring and fracture evolution of polyolefin and steel fibre concrete beams using integrated acoustic emission and digital image correlation techniques, Constr. Build. Mater. 395 (2023) 132306, https://doi.org/10.1016/j.conbuildmat.2023.132306.
[66] L. Weng, Z. Wu, Q. Liu, Z. Wang, Energy dissipation and dynamic fragmentation of dry and water-saturated siltstones under sub-zero temperatures, Eng. Fract. Mech. 220 (2019) 106659, https://doi.org/10.1016/j.engfracmech.2019.106659.
[67] H. Ren, T. Li, J. Ning, S. Song, Analysis of damage characteristics of steel fiber-reinforced concrete based on acoustic emission, Eng. Fail. Anal. 148 (2023) 107166, https://doi.org/10.1016/j.engfailanal.2023.107166.